Transient Characteristics and Quantitative Analysis of Electromotive Force for DFIG-based Wind Turbines during Grid Faults*

Yumei Ma[1], *Donghai Zhu*[1*], *Xudong Zou*[1], *Yong Kang*[1] *and Josep M. Guerrero*[2]
(1. Key Laboratory of Power Electronics and Energy Management for Ministry of Education of China, Huazhong University of Science and Technology, Wuhan 430074, China;
2. Department of Energy Technology, Aalborg University, Aalborg 9220, Denmark)

Abstract: For doubly-fed induction generator (DFIG)-based wind turbines (WTs), various advanced control schemes have been proposed to achieve the low voltage ride through (LVRT) capability, whose parameters design is significantly reliant on the rotor electromotive force (EMF) of DFIG-based WTs. However, the influence of the rotor current on EMF is usually ignored in existing studies, which cannot fully reflect the transient characteristics of EMF. To tackle with this issue, this study presents a comprehensive and quantitative analysis of EMF during grid faults considering various control modes. First, the DFIG model under grid faults is established. Subsequently, the transient characteristics of EMF are analyzed under different control modes (that is, rotor open-circuit and connected to converter). Furthermore, the EMF transient eigenvolumes (that is, accessorial resistance item, transient decay time constant, and frequency offset) are quantitatively analyzed with the typical parameters of MW-level DFIG-based WT. The analysis results contribute to the design of the LVRT control scheme. Finally, the analysis is validated by the hardware-in-the-loop experiments.

Keywords: Doubly-fed induction generator (DFIG), electromotive force (EMF), quantitative analysis, transient characteristics, wind turbines (WTs), grid faults

1 Introduction

With the increasing penetration of wind power into the grid, the safety and stability of wind turbines (WTs) have become increasingly important [1-2]. Thus, transmission operators have formulated stringent grid codes. One of the most demanding requirements is the low voltage ride through (LVRT) capability [3], that is, when a grid fault occurs, the wind turbine should remain connected to the grid and even provide reactive power support.

Doubly-fed induction generator (DFIG)-based WT is one of the mainstream WT types in the market owing to the advantages of variable-speed constant-frequency operation and high-energy efficiency [4]. However, DFIG is sensitive to grid voltage fluctuations because the stator of DFIG is directly tied to the grid [5]. When a grid fault occurs, a large electromotive force (EMF) will be provoked in the rotor circuit, which may lead to rotor overcurrent, dc bus overvoltage, and even damage to the converter if no effective measure is taken [6].

To tackle aforesaid issues, various advanced LVRT controls have been proposed for DFIG-based WTs to suppress EMF disturbance. In Ref. [7], a feedforward transient current control is proposed, in which the rotor voltage is aligned with the EMF to avoid overcurrent. Further, the virtual impedance [8] and robust controller [9] are introduced to reduce the negative effects of EMF disturbance on the control system. However, these methods require a higher rotor voltage and are not suitable for severe grid faults. Consequently, some studies exploited the voltage drop of rotor transient inductance to suppress EMF disturbance. In Ref. [10], the demagnetizing current is injected into the rotor circuit; thus, the voltage drop on

Manuscript received March 30, 2022; revised May 5, 2022; accepted May 11, 2022. Date of publication June 30, 2022; date of current version June 10, 2022.
* Corresponding Author, E-mail: zhudh@hust.edu.cn
* Supported in part by the National Natural Science Foundation of China under Grant 51907072, in part by the Fundamental Research Funds for the Central Universities under Grant 2021XXJS004.
Digital Object Identifier: 10.23919/CJEE.2022.000010

the rotor transient inductance can be increased to offset the EMF and the required rotor voltage is reduced. Similarly, Ref. [11] proposes an inductance-emulating control to implement LVRT, wherein the EMF amplitude is utilized. In addition, the rotor current is controlled to track the transient component of the stator flux [12]. These methods can significantly reduce the rotor voltage requirements and expand the LVRT operating area because they introduce the transient component into the rotor circuit. Furthermore, the EMF has a significant influence on the aforementioned LVRT control schemes; the transient characteristics of EMF are worth exploring, to better design the control parameters.

Numerous studies on the transient characteristic analysis of DFIG-based WT under grid faults have been conducted. In Ref. [13], the dynamic behavior of the stator flux under rotor open-circuit is analyzed. In Ref. [14], the analytical formulas to express the transient characteristics under crowbar protection are provided. In Refs. [15-16], the dynamic performance of stator flux considering the rotor current is analyzed and as indicated, the dynamic performance of the stator flux is determined by simultaneously varying the stator voltage and rotor current. These analyses mainly focus on the dynamic behavior of stator flux; however, they cannot accurately reflect the transient characteristics of the EMF, which is the derivation of stator flux. Thus, Ref. [17] presented the analytical expression of rotor EMF under grid faults, indicating that its amplitude is larger and contains multiple frequency components compared with the normal condition. However, the analysis mainly focuses on the rotor open-circuit condition and subsequent studies have followed this conclusion, the rotor open-circuit voltage is assumed as the EMF and the influence of rotor current on the EMF is ignored [18]. Obviously, the EMF is related to the rotor condition because the stator flux is influenced by the rotor current. Therefore, the transient characteristics of the EMF remain unclear when the rotor current is considered.

Consequently, this study investigates the transient characteristics of the EMF during grid faults, while considering the effect of rotor current. In addition, the transient eigenvolumes based on the typical MW-level DFIG parameters are quantitatively analyzed. Different from the analysis of stator flux, the comprehensive analysis of the EMF is more convenient for the parameters design of LVRT strategies.

The remainder of this paper is organized as follows. In Section 2, the DFIG model under grid faults is proposed. In Section 3, the transient characteristics of the EMF under various rotor-side control modes are analyzed. In Section 4, the quantitative analysis of EMF transient eigenvolumes with typical MW-level DFIG parameters is proposed. The hardware-in-the-loop (HIL) experimental results are provided to validate the aforementioned analysis in Section 5. Finally, some conclusions are summarized in Section 6.

2 DFIG-based WT model under grid faults

For simplicity, all variables are referred to the stator, and both stator and rotor currents adopt the motor convention. The voltage and flux equations of DFIG can be expressed as follows [19]

$$\begin{cases} \boldsymbol{u}_s^s = R_s \boldsymbol{i}_s^s + \dfrac{\mathrm{d}}{\mathrm{d}t}\boldsymbol{\psi}_s^s \\ \boldsymbol{u}_r^r = R_r \boldsymbol{i}_r^r + \dfrac{\mathrm{d}}{\mathrm{d}t}\boldsymbol{\psi}_r^r \end{cases} \tag{1}$$

$$\begin{cases} \boldsymbol{\psi}_s^s = L_s \boldsymbol{i}_s^s + L_m \boldsymbol{i}_r^s \\ \boldsymbol{\psi}_r^r = L_r \boldsymbol{i}_r^r + L_m \boldsymbol{i}_s^r \end{cases} \tag{2}$$

where $\boldsymbol{u}$, $\boldsymbol{i}$, and $\boldsymbol{\psi}$ are the voltage, current, and flux vectors, respectively. R and L are the resistance and inductance, respectively. L_m is the magnetizing inductance. Subscripts "s" and "r" denote the stator and rotor variables whereas superscripts "s" and "r" denote stator and rotor reference frame, respectively. The transformation relationship between the stator and rotor reference frame can be expressed as follows

$$\boldsymbol{X}^s = \boldsymbol{X}^r \exp(j\theta) \tag{3}$$

where $\boldsymbol{X}$ denotes variables in the form of the space vector and θ is the rotor position angle.

According to Eq. (2), the stator current can be derived as

$$\boldsymbol{i}_s^s = \frac{\boldsymbol{\psi}_s^s - L_m \boldsymbol{i}_r^s}{L_s} \tag{4}$$

Substituting Eq. (4) into Eq. (1), the stator flux equation can be derived as

$$\frac{\mathrm{d}}{\mathrm{d}t}\boldsymbol{\psi}_s^s+\frac{R_s}{L_s}\boldsymbol{\psi}_s^s=\boldsymbol{u}_s^s+k_{ms}R_s\boldsymbol{i}_r^s \tag{5}$$

where $k_{ms}= L_m/L_s$. As seen, the stator flux is influenced by stator voltage and rotor current simultaneously.

Similarly, by substituting Eq. (3) into Eq. (2), the rotor flux can be derived as

$$\boldsymbol{\psi}_r^r=k_{ms}\boldsymbol{\psi}_s^r+\sigma L_r\boldsymbol{i}_r^r \tag{6}$$

Combining Eq. (6) with Eq. (1), the rotor voltage can be derived as

$$\boldsymbol{u}_r^r=\underbrace{k_{ms}\frac{\mathrm{d}}{\mathrm{d}t}\boldsymbol{\psi}_s^r}_{\boldsymbol{e}_r^r}+(R_r+\sigma L_r\frac{\mathrm{d}}{\mathrm{d}t})\boldsymbol{i}_r^r \tag{7}$$

where σ is the leakage factor and $\sigma=1-L_m^2/(L_sL_r)$. As shown in Eq. (7), the rotor voltage can be decomposed into two items: the rotor EMF and the voltage drop across R_r and σL_r . Furthermore, the equivalent circuit of DFIG can be drawn, as shown in Fig. 1.

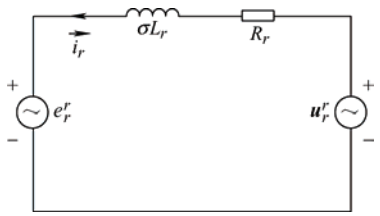

Fig. 1 Equivalent circuit of DFIG

3 Transient characteristics of EMF under various rotor-side control modes

When a symmetrical grid fault occurs at t_0, the stator voltage can be expressed as follows

$$\boldsymbol{u}_s^s=\begin{cases}V_s\exp(j\omega_s t) & t<t_0\\ (1-h)V_s\exp(j\omega_s t) & t\geqslant t_0\end{cases} \tag{8}$$

where V_s is the rated stator voltage, ω_s is the stator angular frequency, and h is the depth of grid voltage dip.

3.1 Rotor open-circuit

Under this condition, the rotor current is zero. Thus, the stator flux equation (5) can be rewritten as

$$\frac{\mathrm{d}}{\mathrm{d}t}\boldsymbol{\psi}_s^s=\boldsymbol{u}_s^s-\frac{R_s}{L_s}\boldsymbol{\psi}_s^s \tag{9}$$

Substituting Eq. (8) into Eq. (9), the stator flux under normal conditions can be expressed as follows

$$\boldsymbol{\psi}_s^s=\frac{\boldsymbol{u}_s^s}{R_s/L_s+j\omega_s}=\frac{V_s\exp(j\omega_s t)}{R_s/L_s+j\omega_s} \tag{10}$$

Because $R_s/L_s\ll\omega_s$, the stator flux can be simplified as

$$\boldsymbol{\psi}_s^s\approx\frac{\boldsymbol{u}_s^s}{j\omega_s}=\frac{V_s\exp(j\omega_s t)}{j\omega_s} \tag{11}$$

According to Eq. (7) and Eq. (11), the EMF can be derived as

$$\boldsymbol{e}_r^r=\frac{\mathrm{d}}{\mathrm{d}t}\boldsymbol{\psi}_s^r=k_{ms}\xi V_s\exp(j\omega_2 t) \tag{12}$$

where $\omega_2=\omega_s-\omega_r$ is the slip angular frequency and $\xi=\omega_2/\omega_s$ is the slip. The DFIG operates under normal conditions usually with a small speed range, that is, with a small slip, typically less than ±0.3. Thus, the EMF will not exceed 30% of the rated stator voltage.

However, when a symmetrical grid fault occurs, the stator flux will contain positive-sequence and transient components caused by voltage dips. These components can be calculated by the solutions of the stator flux equation (Eq. (5)), where particular and general solutions correspond to the steady-state and transient components of stator flux [20]. Solving Eq. (9), the positive-sequence steady-state component of the stator flux can be deduced as

$$(\boldsymbol{\psi}_s^s)^p\approx\frac{(1-h)\boldsymbol{u}_s^s}{j\omega_s}=\frac{(1-h)V_s\exp(j\omega_s t)}{j\omega_s} \tag{13}$$

where superscript p represents the positive-sequence component. Similarly, superscripts n and d represent negative-sequence and transient components, respectively.

Because the stator flux linkage cannot mutate, the transient component can be obtained using the general solution of Eq. (9), which is deduced as

$$(\boldsymbol{\psi}_s^s)^d\approx\frac{hV_s\exp(-\lambda_s t)}{j\omega_s} \tag{14}$$

where λ_s represents the decay rate of the transient component of stator flux, which can be expressed as follows

$$\lambda_s=\frac{R_s}{L_s} \tag{15}$$

According to Eq. (13) and Eq. (14), the stator flux can be derived as follows

$$\boldsymbol{\psi}_s^s=(\boldsymbol{\psi}_s^s)^p+(\boldsymbol{\psi}_s^s)^d\approx\frac{(1-h)V_s\exp(j\omega_s t)}{j\omega_s}+\frac{hV_s\exp(-\lambda_s t)}{j\omega_s} \tag{16}$$

Combining Eq. (16) with Eq. (7), the EMF can be

derived as follows

$$\boldsymbol{e}_r^r \approx \underbrace{k_{ms}\xi(1-h)V_s\exp(j\omega_2 t)}_{(\boldsymbol{e}_r^r)^p} + \underbrace{k_{ms}(\xi-1)hV_s\exp\left(-j\omega_r t-\frac{R_s}{L_s}t\right)}_{(\boldsymbol{e}_r^r)^d} \tag{17}$$

Comparing Eq. (12) with Eq. (17), the amplitude and frequency of EMF are both seen to be different from the normal condition. The analysis is as follows.

The amplitude of the EMF under severe grid faults is usually several times its normal values. For instance, under a zero-voltage fault with ξ=−0.3, the initial EMF amplitude according to Eq. (17) is $1.3k_{ms}V_s$, which is 4.3 multiples of its normal values according to Eq. (12). In addition, the initial EMF amplitude will also exceed the dc bus voltage which is designed according to normal conditions.

As seen in Eq. (17), the frequency of the positive-sequence and transient component of the EMF are ω_2 and ω_r, respectively. Therefore, when the EMF is transferred into a synchronous coordinate system, the positive-sequence and transient components are expressed as a DC quantity and a fundamental frequency AC quantity, respectively. For the traditional PI controller, AC components cannot be accurately tracked [21]. Thus, the effective suppression of the disturbance caused by the EMF transient component is difficult. Further, in the case of a minor grid fault in which the amplitude of the EMF is lower than the DC bus, the rotor side converter (RSC) may fail to output a suitable voltage to offset the EMF owing to the limited tracking ability of the controller.

3.2 Rotor connected to converter

When a severe grid fault occurs, the large fault current will flow into the rotor circuit, which will impact the transient characteristics of the stator flux and EMF. According to Eq. (5), when the influence of rotor current is considered, the positive-sequence of stator flux can be written as

$$\frac{\mathrm{d}}{\mathrm{d}t}(\boldsymbol{\psi}_s^s)^p + \frac{R_s}{L_s}(\boldsymbol{\psi}_s^s)^p = (\boldsymbol{u}_s^s)^p + k_{ms}R_s(\boldsymbol{i}_r^s)^p \tag{18}$$

The positive-sequence of stator flux can be expressed as

$$(\boldsymbol{\psi}_s^s)^p = \left|(\boldsymbol{\psi}_s^s)^p\right|\exp(j\omega_s t) \tag{19}$$

where $\left|(\boldsymbol{\psi}_s^s)^p\right|$ is the amplitude of the positive component of the stator flux. Hence, the derivative of the positive-sequence of the stator flux can be deduced as

$$\frac{\mathrm{d}}{\mathrm{d}t}(\boldsymbol{\psi}_s^s)^p = \left|(\boldsymbol{\psi}_s^s)^p\right|\exp(j\omega_s t)j\omega_s = j\omega_s(\boldsymbol{\psi}_s^s)^p \tag{20}$$

Substituting Eq. (20) into Eq. (18), the positive-sequence component of the stator flux can be derived as

$$(\boldsymbol{\psi}_s^s)^p = \frac{(\boldsymbol{u}_s^s)^p + k_{ms}R_s(\boldsymbol{i}_r^s)^p}{j\omega_s + R_s/L_s} \tag{21}$$

Similarly, the negative-sequence component of stator flux can be derived as

$$(\boldsymbol{\psi}_s^s)^n = \frac{(\boldsymbol{u}_s^s)^n + k_{ms}R_s(\boldsymbol{i}_r^s)^n}{-j\omega_s + R_s/L_s} \tag{22}$$

As seen in Eq. (21) and Eq. (22), the stator flux is related to the rotor current. To quantitatively analyze the influence, the transient component of rotor current is decomposed into two quadrature components (parallel and perpendicular to the stator flux). The transient component of the rotor current can be expressed as follows

$$(\boldsymbol{i}_r^s)^d = (k_a + jk_b)\left(\frac{\boldsymbol{\psi}_s^s}{L_m}\right)^d = (k_a + jk_b)(\boldsymbol{i}_{sm}^s)^d = k_a(\boldsymbol{i}_{sm}^s)^d + jk_b(\boldsymbol{i}_{sm}^s)^d \tag{23}$$

where $\boldsymbol{i}_{sm}^s = \boldsymbol{\psi}_s^s/L_m$ and $\boldsymbol{i}_{sm}^s$ are the equivalent excitation currents corresponding to the stator flux. k_a and k_b represent the projection value of the components parallel and perpendicular to stator flux, respectively.

The transient component of stator flux can be deduced by solving Eq. (5). Substituting Eq. (20) into Eq. (5), the decay rate of the transient component in the stator flux can be calculated as

$$\lambda_s = \left(\frac{R_s}{L_s} - \frac{R_s}{L_s}k_a\right) - j\frac{R_s}{L_s}k_b \tag{24}$$

The transient component of the stator flux can be derived as

$$(\boldsymbol{\psi}_s^s)^d = \psi_{s0}\exp(-\lambda_s t) = \psi_{s0}\exp\left(-\frac{R_s}{L_s}(1-k_a)t + j\frac{R_s}{L_s}k_b t\right) \tag{25}$$

where ψ_{s0} is the initial value of the stator flux. Finally, Eqs. (21), (22), and (25) constitute the positive-, negative-sequence, and transient components of the

stator flux, respectively. According to the definition of EMF in Eq. (7), the corresponding EMF components can be derived as

$$(\boldsymbol{e}_r^r)^p \approx \xi k_{ms}(\boldsymbol{u}_s^r)^p + \xi k_{ms}^2 R_s(\boldsymbol{i}_r^r)^p \quad (26)$$

$$(\boldsymbol{e}_r^r)^n \approx (2-\xi)k_{ms}(\boldsymbol{u}_s^r)^n + (2-\xi)k_{ms}^2 R_s(\boldsymbol{i}_r^r)^n \quad (27)$$

$$(\boldsymbol{e}_r^r)^d = k_{ms}(-\frac{R_s}{L_s} - j\omega_r)(\boldsymbol{\psi}_s^s)^d \exp(-j\theta) + k_{ms}^2 R_s(\boldsymbol{i}_r^r)^d \quad (28)$$

As seen, all EMF components are added with an accessorial resistance term proportional to the rotor current (e.g., $\xi k_{ms}^2 R_s(\boldsymbol{i}_r^r)^p$). In addition, the decay rate of the EMF transient component is also influenced. According to Eq. (25), the transient component of the stator flux decays at a speed of $(1-k_a)R_s/L_s$ and the frequency alternates at a speed of $(k_b R_s/L_s)$. Thus, the influence of the rotor current on the rotor EMF can be summarized as follows.

(1) An accessorial resistance item proportional to the rotor current is generated in the positive-sequence, negative-sequence, and transient components of the EMF.

(2) The decay rate and alternating frequency of the EMF transient component differ from the rotor open-circuit condition.

4 Quantitative analysis of EMF transient eigenvolumes

According to the analysis in Section 3, when the influence of rotor current is considered, the transient eigenvolumes such as the accessorial resistance item, decay rate, and frequency offset will be influenced. To quantitatively analyze the influence, typical parameters of MW-level DFIG are summarized and the ranges of EMF transient eigenvolumes' variation under allowable operation modes are clarified.

4.1 Typical parameters of MW-level DFIG

The typical MW-level DFIG parameters of domestic wind turbine manufacturers and previous studies are investigated, as shown in Tab. 1 and Tab. 2 [21-30].

Tab. 1 Typical MW-level DFIG parameters of domestic wind turbine manufactures

Manufacturers	Capacity/MW	R_s/p.u.	R_r/p.u.	L_{1s}/p.u.	L_{1r}/p.u.	$\omega_s\sigma L_s/R_s$
Lanzhou Electric Corporation	1.5	0.007 6	0.010 4	0.111 1	0.094 6	27.17
Dalian Tianyuan Electrical Machinery Co., Ltd.	1.5	0.006 5	0.005 2	0.052 0	0.187 9	36.80
Dongfang Electric Corporation	1.5	0.008 1	0.010 7	0.146 5	0.096 4	29.80
CRRC Yongji Electric Co., Ltd.	1.5	0.005 8	0.006 7	0.092 5	0.170 0	45.03
Nanyang Electric Corporation	1.5	0.006 1	0.006 5	0.088 2	0.132 8	36.30
Xiangtan Electric Manufacturing Co., Ltd.	1.5	0.010 9	0.008 5	0.055 3	0.196 0	22.95
Dunan Electric Corporation	1.5	0.010 1	0.009 8	0.075 5	0.117 5	19.12
Nanjing Turbine & Electric Machinery Co., Ltd.	2.0	0.008 7	0.007 6	0.135 9	0.089 2	25.97

Tab. 2 Typical MW-level DFIG parameters of previous studies

Literature	Capacity/MW	R_s/p.u.	R_r/p.u.	L_{1s}/p.u.	L_{1r}/p.u.	$\omega_s\sigma L_s/R_s$
Ref. [21]	1.50	0.007	0.005	0.171	0.156	46.71
Ref. [22]	1.50	0.008	0.008	0.167	0.132	37.38
Ref. [23]	1.50	0.006	0.007	0.171	0.156	54.50
Ref. [24]	1.50	0.007 6	0.005	0.171	0.156	43.03
Ref. [25]	1.50	0.011	0.009	0.175	0.158	30.27
Ref. [26]	1.50	0.003	0.003	0.11	0.07	60
Ref. [16]	1.67	0.007	0.009	0.171	0.156	46.71
Ref. [27]	1.76	0.007 06	0.005	0.17	0.156	46.18
Ref. [9]	2.00	0.01	0.009	0.18	0.07	25
Ref. [28]	2.00	0.004 91	0.005 52	0.092 73	0.1	39.25
Ref. [29]	2.00	0.007 4	0.006 1	0.102 2	0.112 3	28.99
Ref. [30]	2.50	0.006	0.010	0.161	0.144	50.83

According to the typical MW-level DFIG parameters in Tab. 1 and Tab. 2, ① The per-unit values of stator and rotor resistances are between 0.003 p.u. and 0.011 p.u., and these values typically range from 0.005 p.u. to 0.01 p.u. ② The sum of the stator and rotor leakage inductances (L_{1s}+L_{1r}) ranges from 0.18 p.u. to 0.333 p.u.; this value typically ranges from 0.25 p.u. to 0.33 p.u. ③ The short circuit impedance ratio ($\omega_s\sigma L_s/R_s$) ranges from 19.12 to 60. This value typically ranges from 25 to 40. Notably, the aforementioned parameters are suitable for MW-level DFIG. Because this study is mainly aimed at high-power WTs, $R_s\in$[0.005 p.u., 0.01 p.u.], $\sigma L_s\in$[0.25 p.u., 0.33 p.u.], and $\sigma L_s/R_s\in$[25, 40] are selected as the benchmark for the undermentioned quantitative analysis.

4.2 Ranges of EMF transient eigenvolumes' variation

The transient eigenvolumes including the accessorial resistance item, transient decay time constant, and frequency offset are quantitatively analyzed as follows.

(1) Accessorial resistance item: According to Eqs. (26), (27), and (28), when the stator resistance R_s=0.01 p.u., rotor transient inductance σL_r=0.3 p.u., and the slip ξ=−0.3, the accessorial resistance items of positive-sequence, transient, and negative-sequence components are −0.003 p.u., 0.01 p.u., and 0.023 p.u., respectively. Whereas, the inductive reactance corresponding to the rotor transient inductance are 0.09 p.u., 0.39 p.u., and 0.69 p.u., respectively. As seen, the additional resistance item is much smaller than the inductive reactance.

(2) Transient decay time constant: The transient decay time constant can be calculated as $\tau_s=1/\lambda_s$. According to Eq. (15) and Eq. (24), the transient decay time constant is changed from L_s/R_s to $L_s/R_s(1-k_a)$ when the influence of rotor current is considered. In addition, the transient decay time constant under crowbar protection with zero resistance is $\sigma L_s/R_s$ [16]. However, the actual transient decay time constant is much larger than $\sigma L_s/R_s$. The reason is twofold: On the one hand, to avoid RSC overcurrent, the rotor current under control is usually within the limit value, which does not exceed the rotor current under crowbar protection. On the other hand, the rotor current is constrained by the RSC output voltage. The amplitude of the rotor current is influenced by the EMF and rotor output voltage. Therefore, when the voltage and current capacity constraints are considered, the transient time constant can be expressed as

$$\tau_s=\frac{1}{\lambda_s}\geqslant\frac{\sigma L_s}{R_s} \tag{29}$$

According to the typical parameters in Section 4.1, $\omega_s\sigma L_s/R_s\in$[25, 40]; thus, the minimum value of τ_s ranges from 80 ms to 127 ms.

(3) Frequency offset: Because the rotor current perpendicular to the stator flux generates an electromagnetic torque, the stator flux will be dragged to rotate and the stator flux transient component has both decay and rotational characteristics in Eq. (25). Correspondingly, the frequency of the EMF in the rotor stationary coordinate system deviates from the rotor rotational frequency. The frequency offset of the EMF transient component depends on the magnitude of the rotor current perpendicular to the stator flux. According to the equivalent circuit of DFIG, the magnitude of the perpendicular rotor current will not exceed

$$\left|k_b\left(\frac{\boldsymbol{\psi}_s^s}{L_m}\right)^d\right|\leqslant\frac{U_{r\max}}{\omega_r\sigma L_r} \tag{30}$$

where $U_{r\max}$ is the maximum value of the rotor output voltage. Correspondingly, the frequency offset of the EMF transient component can be expressed as follows

$$\begin{aligned}\mathrm{Im}(\lambda_s)=\frac{R_s}{L_s}k_b\leqslant\frac{R_s}{L_s}\frac{\frac{U_{r\max}}{\omega_r\sigma L_r}}{hV_s/\omega_sL_m}\approx\\ \frac{R_s}{\sigma L_r}\frac{U_{r\max}^*}{(1-\xi)h}<\frac{R_s^*}{\sigma L_r^*}\omega_s\end{aligned} \tag{31}$$

where the superscripts "*" denotes the per-unit values. According to the parameters in Section 4.1, the maximum frequency offset will not exceed 2.5 Hz.

Generally, the rotor current has a significant influence on the transient characteristics of the EMF, particularly the accessorial resistance item, transient decay time constant, and frequency offset. However, when the amplitude of the first fundamental cycle period is concerned, the EMF amplitude suffers a little influence no matter what control strategy is used because $\tau_s\geqslant$80 ms and the amplitude decay cannot

exceed 20%. Therefore, if the hardware of the DFIG is unchanged, overvoltage and overcurrent should be suppressed using the RSC control to comply with the EMF transient characteristics instead of changing them.

5 Experimental verification

To validate the analysis in Section 4, HIL experiments are conducted, as shown in Fig. 2. The main circuit of DFIG and network run in a high-speed real-time simulator (SpaceR) with a step size of 20 μs. The entire control of DFIG is implemented in two DSP controllers (TMS320F28335), the switching frequency f_{sw} is 10 kHz. Signals such as voltage and current are output to the I/O box that connects the HIL simulator and DSP controller. A more detailed description of the experimental setup has been provided in Ref. [31]. The system parameters are listed in Tab. 3.

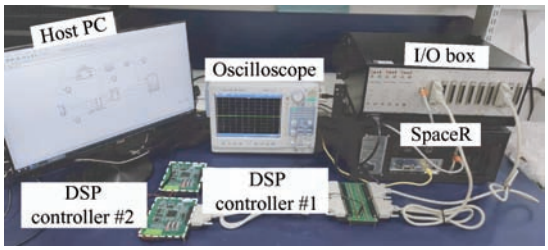

Fig. 2 Photo of the HIL experimental setup

In the experiments, the DFIG operates at the sub-synchronous speed, that is, ξ =0.3. Under the normal operating condition, the conventional PQ control is used. When the grid voltage drops by 100%, that is, h=1.0, the conventional PQ control and current reverse tracking control [32] (equivalent k_a=−0.89) are used simultaneously.

Tab. 3 System parameters of a 1.5 MW DFIG-based WT

Parameter	Value
Rated power/MW	1.5
Rated stator voltage/V	690
Rated frequency/Hz	50
Pairs of poles	2
Turn ratio	0.4
Stator resistance/p.u.	0.007
Stator leakage inductance/p.u.	0.171
Magnetizing inductance/p.u.	2.902
Rotor resistance/p.u.	0.005
Rotor leakage inductance/p.u.	0.156
Rated DC-bus voltage/V	1 200

For the conventional PQ control, the current reference is maintained as the DC component during grid faults. As seen in Fig. 3a, an obvious transient component can be observed in the rotor current, meaning it cannot accurately track the reference owing to the limitation of the RSC voltage output capability. In addition, the EMF under the synchronized coordinate system contains a significant 50 Hz component whose amplitude decays slowly. This component still exists at 300 ms after the grid fault.

As seen in Fig. 3b, when the current reverse tracking control is used, the transient component of EMF decays rapidly compared with the conventional PQ control. As seen, the transient decay of the EMF is significantly related to the RSC control strategy. However, the difference between different strategies is not obvious in the first fundamental cycle after the grid fault. The aforementioned experimental results under different strategies validate the theoretical analysis in Section 4.

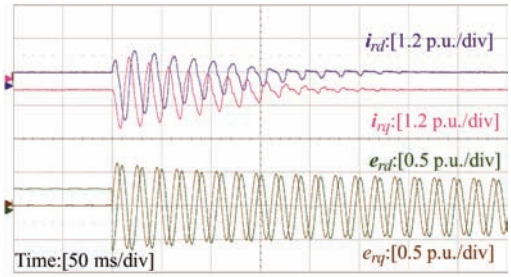

(a) Conventional PQ control

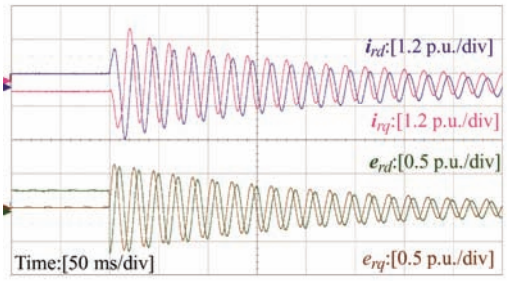

(b) Current reverse tracking control

Fig. 3 Experimental results of the *dq* components of the rotor current and EMF under different control strategies

6 Conclusions

In this study, the transient characteristics and quantitative analysis of the EMF for DFIG-based WT during grid faults was presented. The main conclusions can be summarized as follows.

(1) The rotor current had a significant influence on the transient characteristics of the EMF, particularly

the accessorial resistance item, the transient decay time constant, and the frequency offset.

(2) Owing to the typical parameters of MW-level DFIG, the rotor current had a limited impact on the amplitude and frequency of the EMF transient component in the first fundamental cycle after the grid fault. Thus, RSC control during this period should conform to the EMF instead of changing it.

References

[1] Y Li, L Fan, Z Miao. Wind in weak grids: Low-frequency oscillations, subsynchronous oscillations, and torsional interactions. *IEEE Transactions on Power Systems*, 2020, 35(1): 109-118.

[2] X Guo, D Zhu, J Hu, et al. Inertial PLL of grid-connected converter for fast frequency support. *CSEE Journal of Power and Energy Systems*, doi: 10.17775/CSEEJPES.2021.08650.

[3] M Tsili, S Papathanassiou. A review of grid code technical requirements for wind farms. *IET Renewable Power Generation*, 2009, 3(3): 308-332.

[4] Z Din, J Zhang, Z Xu, et al. Low voltage and high voltage ride-through technologies for doubly fed induction generator system: Comprehensive review and future trends. *IET Renewable Power Generation*, 2021, 15(3): 614-630.

[5] D Zhou, F Blaabjerg. Optimized demagnetizing control of DFIG power converter for reduced thermal stress during symmetrical grid fault. *IEEE Transactions on Power Electronics*, 2018, 33(12): 10326-10340.

[6] X Zou, D Zhu, J Hu, et al. Mechanism analysis of the required rotor current and voltage for DFIG-based WTs to ride-through severe symmetrical grid faults. *IEEE Transactions on Power Electronics*, 2018, 33(9): 7300-7304.

[7] J Liang, W Qiao, R G Harley. Feed-forward transient current control for low-voltage ride-through enhancement of DFIG wind turbines. *IEEE Transactions on Energy Conversion*, 2010, 25(3): 836-843.

[8] Z Xie, X Zhang, X Zhang, et al. Improved ride-through control of DFIG during grid voltage swell. *IEEE Transactions on Industrial Electronics*, 2015, 62(6): 3584-3594.

[9] J P Da Costa, H Pinheiro, T Degner, et al. Robust controller for DFIGs of grid-connected wind turbines. *IEEE Transactions on Industrial Electronics*, 2011, 58(9): 4023-4038.

[10] L Zhou, J Liu, S Zhou. Improved demagnetization control of a doubly-fed induction generator under balanced grid fault. *IEEE Transactions on Power Electronics*, 2014, 30(12): 6695-6705.

[11] D Zhu, X Zou, D Lu, et al. Inductance-emulating control for DFIG-based wind turbine to ride-through grid faults. *IEEE Transactions on Power Electronics*, 2017, 32(11): 8514-8525.

[12] L Ran, D Xiang, P J Tavner, et al. Control of a doubly fed induction generator in a wind turbine during grid fault ride-through. *IEEE Power Engineering Society General Meeting*, 18-22 June 2006, Montreal, QC, Canada. IEEE, 2006.

[13] J Lopez, P Sanchis, X Roboam, et al. Dynamic behavior of the doubly fed induction generator during three-phase voltage dips. *IEEE Transactions on Power Electronics*, 2007, 22(3): 709-717.

[14] S Yang, T Zhou, L Chang, et al. Analytical method for DFIG transients during voltage dips. *IEEE Transactions on Power Electronics*, 2017, 32(9): 6863-6881.

[15] R Zhu, Z Chen, X Wu, et al. Dynamic performance of doubly-fed induction generator stator flux during consecutive grid voltage variations. *IET Renewable Power Generation*, 2015, 9(7): 720-728.

[16] S Zhou, D Zhu, Y Yang, et al. Analysis and assessment of stator flux attenuation time-scales of type-3 wind turbines with different LVRT control modes. *2020 IEEE 9th International Power Electronics and Motion Control Conference (IPEMC2020-ECCE Asia)*, 2020: 1162-1166.

[17] G Abed, J Lopez, M A Rodnguez, et al. Doubly fed induction machine: Modeling and control for wind energy generation applications. Piscataway: IEEE Press, 2012.

[18] S Xiao, G Yang, H Zhou, et al. An LVRT control strategy based on flux linkage tracking for DFIG-based WECS. *IEEE Transactions on Industrial Electronics*, 2013, 60(7): 2820-2832.

[19] F K A Lima, A Luna, P Rodriguez, et al. Rotor voltage dynamics in the doubly fed induction generator during grid faults. *IEEE Transactions on Power Electronics*, 2010, 25(1): 118-130.

[20] J LÓpez, E Gubía, P Sanchis, et al. Wind turbines based on doubly fed induction generator under asymmetrical voltage dips. *IEEE Transactions on Energy Conversion*, 2008, 23(1): 321-330.

[21] D Zhu, X Zou, S Zhou, et al. Feedforward current

references control for DFIG-based wind turbine to improve transient control performance during grid faults. *IEEE Transactions on Energy Conversion*, 2018, 33(2): 670-681.

[22] X Zhang, D Xu, W Pan, et al. A flux damping control strategy of doubly-fed induction generator based on the grid voltage vector oriented. *Automation of Electric Power System*, 2020, 34(7): 95-99.

[23] Z Zheng, G Yang, H Geng. Short circuit current analysis for DFIG-based wind generation system with crowbar protection under grid faults. *Electric Power Automation Equipment*, 2012, 32(11): 7-15.

[24] X Wang, W Sun. Simulation study on dynamic response of doubly fed induction generators during system voltage sag caused by power grid faults. *Power System Technology*, 2010, 34(8): 170-175.

[25] H Ma, Y Gao, Y Yang, et al. Fuzzy optimization of crowbar resistance for low-voltage ride trough of doubly fed induction generators. *Proceedings of the CSEE*, 2012, 32(34): 17-23.

[26] W Guo, L Xiao, S Dai. Enhancing low-voltage ride-through capability and smoothing output power of DFIG with a superconducting fault-current limiter -magnetic energy storage system. *IEEE Transactions on Energy Conversion*, 2012, 27(2): 277-295.

[27] M Rahimi, M Parniani. Transient performance improvement of wind turbines with doubly fed induction generators using nonlinear control strategy. *IEEE Transactions on Energy Conversion*, 2010, 25(2): 514-525.

[28] J Hu, D Sun, Y He, et al. Modeling and control of DFIG wind energy generation system under grid voltage dip. *Automation of Electric Power Systems*, 2006, 30(8): 21-26.

[29] M Firouzi, G B Gharehpetian. LVRT performance enhancement of DFIG-based wind farms by capacitive bridge-type fault current limiter. *IEEE Transactions on Sustainable Energy*, 2018, 9(3): 1118-1125.

[30] Y Yang, D Zhu, X Zou, et al. Power compensation control for DFIG-based wind turbines to enhance synchronization stability during severe grid faults. *IEEE Transactions on Power Electronics*, 2022, 37(9): 10139-10143.

[31] X Guo, D Zhu, X Zou, et al. Analysis and enhancement of active power transfer capability for DFIG-based WTs in very weak grid. *IEEE Journal of Emerging and Selected Topics in Power Electronics*, 2021. doi: 10.1109/JESTPE.2021.3089235.

[32] Q Huang, M Sun, X Zou, et al. A reverse current tracking based LVRT strategy for doubly fed induction generator (DFIG). *Proceedings of the 39th Annual Conference of Industrial Electronics Society (IECON)*, 2013: 728-735.

Yumei Ma (Student Member, IEEE) was born in Dezhou, China, in 1999. She received the B.S. degree in Electrical Engineering from Guizhou University, Guiyang, China, in 2020. She is currently working toward the Ph.D. degree with the School of Electrical and Electronic Engineering, Huazhong University of Science and Technology, Wuhan, China.

Her current research interests include renewable energy generation systems, stability and power quality of converter-based power systems.

Donghai Zhu (Member, IEEE) was born in Anhui, China. He received the Ph.D. degree in Electrical Engineering from the Huazhong University of Science and Technology, Wuhan, China, in 2018.

He is currently an Associate Professor with the School of Electrical and Electronic Engineering, Huazhong University of Science and Technology, Wuhan. His current research interests include renewable energy generation systems and power electronic converters.

Dr. Zhu was selected for the National Postdoctoral Program for Innovative Talents in 2018 and the Postdoctoral Post for Innovative Research in Hubei Province in 2019. He was a recipient of the *International Journal of Electrical Power and Energy Systems* Outstanding Reviewer in 2018 and the IEEE Transactions on Energy Conversion Best Paper Award in 2019.

Xudong Zou (Member, IEEE) was born in Hunan, China, in 1974. He received the B.S., M.S., and Ph.D. degrees in Electrical Engineering from the Huazhong University of Science and Technology, Wuhan, China, in 1997, 2000, and 2005, respectively

Since 2005, he has been a Faculty Member with the Huazhong University of Science and Technology, where he is currently a Full Professor with the School of Electrical and Electronic Engineering. His current research interests include power electronic converters, renewable energy generation system, and flywheel energy storage.

Dr. Zou was a recipient of the IEEE Transactions on Energy Conversion Best Paper Award in 2019.

Yong Kang (Senior Member, IEEE) was born in Hubei, China, in 1965. He received the B.E., M.E., and Ph.D. degrees in Electrical Engineering from the Huazhong University of Science and Technology, Wuhan, China, in 1988, 1991, and 1994, respectively.

Since 1994, he has been a Faculty Member with the Huazhong University of Science and Technology, where he is currently a Full Professor with the School of Electrical and Electronic Engineering. His research interests include the power electronic converters, ac drivers, and renewable energy generation systems.

Dr. Kang was a recipient of the Delta Scholar Award from the Delta

Environmental and Educational Foundation in 2005, and supported by the Program for New Century Excellent Talents in University from the Chinese Ministry of Education in 2004. In 2017, he was appointed as the Chief Scientist of the National Key R&D Program of China. He was a recipient of the highly prestigious China National Science and Technology Award in 2019. He currently serves as the Vice Chairman of the China UPS Standard Committee and an Associate Editor for the *Journal of Power Electronics*.

Josep M. Guerrero (Fellow, IEEE) received the B.S. degree in Telecommunications Engineering, the M.S. degree in Electronics Engineering, and the Ph.D. degree in Power Electronics from the Technical University of Catalonia, Barcelona, in 1997, 2000, and 2003, respectively. Since 2011, he has been a Full Professor with the Department of Energy Technology, Aalborg University, Denmark, where he is responsible for the Microgrid Research Program. He has been the Chair Professor with Shandong University, since 2014, a Distinguished Guest Professor with Hunan University, since 2015, a Visiting Professor Fellow with Aston University, UK, since 2016, and a Guest Professor with the Nanjing University of Posts and Telecommunications. In 2019, he became a Villum Investigator. He has published more than 500 journal articles in the fields of microgrids and renewable energy systems, which are cited more than 30 000 times. His research interests include oriented to different microgrid aspects, including power electronics, distributed energy storage systems, hierarchical and cooperative control, energy management systems, smart metering, and the Internet of Things for AC/DC microgrid clusters and islanded minigrids, recently specially focused on maritime microgrids for electrical ships, vessels, ferries, and seaports. In 2015, he was elevated as a fellow of IEEE for his contributions on "Distributed power systems and microgrids." He received the Best Paper Award of the IEEE Transactions on Energy Conversion, from 2014 to 2015, and the Best Paper Prize of IEEE-PES, in 2015, and the Best Paper Award of the Journal of Power Electronics, in 2016. For five consecutive years, from 2014 to 2018, he was awarded by Clarivate Analytics (former Thomson Reuters) as the Highly Cited Researcher. He is an associate editor for a number of IEEE Transactions.